The Effect of Microstructural and Rheological Heterogeneity on Porphyroblast Kinematics and Bulk Strength in Porphyroblastic Schists

Frieman, Ben M., Gerbi, Christopher C., Johnson, Scott E.
University of Maine, Department of Earth Sciences,
Orono, Maine, USA; ben.frieman@maine.edu

I. Introduction

– Porphyroblast bearing rocks may be relatively strong (e.g., Groome and Johnson, 2006)
– Or, given weak material proximal to porphyroblasts (e.g., mica) these rocks may be relatively weak (e.g., Johnson et al., 2009)
– Such microstructural and rheological heterogeneity can also influence the partitioning of strain, thus affecting the kinematic behavior of porphyroblasts
– It is unclear how variation in microstructural distributions of rheologically distinct fabric elements affects the bulk strength and kinematic behavior of porphyroblasts
  • i.e., little is known about how rheological heterogeneities that affect bulk strength relate to those that affect porphyroblast-matrix coupling
–» To investigate these complexities we utilized a well-preserved kinematic record of boudinaged staurolite porphyroblasts and supplementary finite element numerical models.

II. Geologic Setting

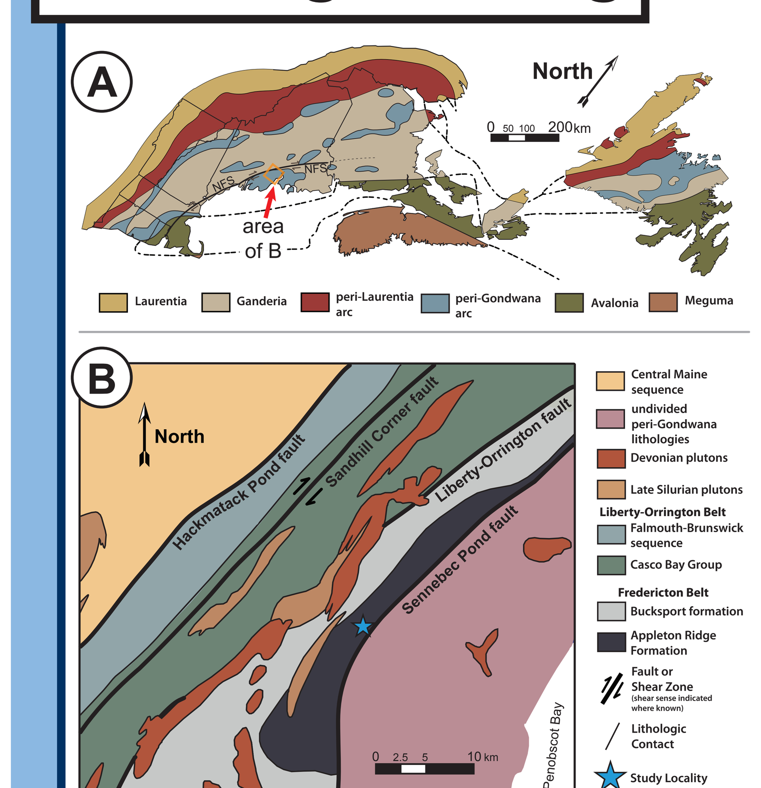

Figure 1. (A) Generalized lithotectonic map of the Northern Appalachians; arrow marks the location of B. (B) Geologic setting of the study area (star); after Hibbard et al. (2006) and Gerbi & West (2007). All faults except the Sennebec Pond fault likely originated as shear zones. NFS=Norumbega fault system.

– Study site (star in Fig. 1B) located in Appleton Ridge Formation, a member of the Fredericton Belt lithotectonic unit
  • metaturbidite sequence
  • rich in andalusite and staurolite
– Regional Silurian-Devonian orogenesis coincident with a protracted history of plutonism, metamorphism, and ductile deformation
– Latest fabric reflects shear at high temperature low pressure conditions

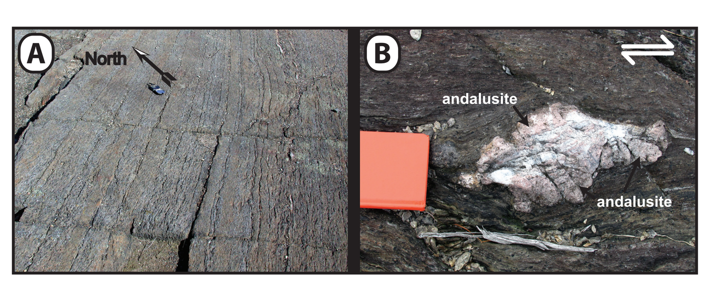

Figure 2. Annotated field photographs displaying general outcrop scale features of the study area. (A) Outcrop view of porphyroblastic schists interbedded with thin psammitic layers that are largely planar in outcrop (photo courtesy of D.P. West). (B) Asymmetrically sheared quatrz pod bearing large pink andalusite, which displays a dextral shear sense; transit book is 12cm top to bottom.

III. Outcrop & Thin Section Observations

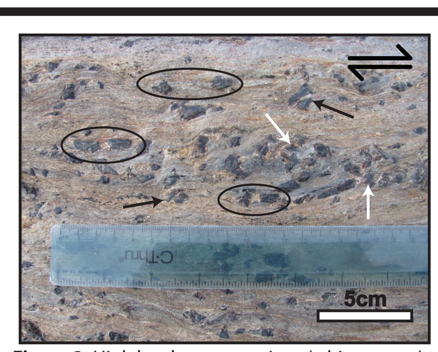

Figure 3. High local concentrations (white arrows), asymmetrical microboudinage (circled areas), and tiling (black arrows) of staurolites porphyroblasts.

– Cm-scale staurolite porphs
– Boudinage of elongate and twinned grains of staurolite
– High local concentrations of porphyroblasts
– No clear preferred orientation of staurolite grains

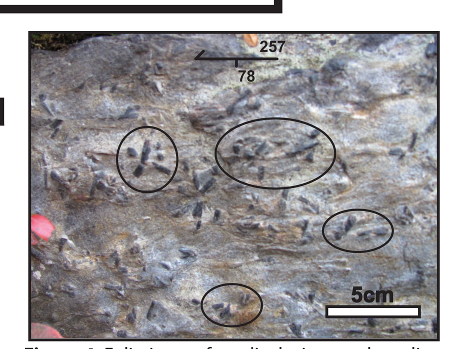

Figure 4. Foliation surface displaying no clear alignment of staurolite porphyroblasts, but several with asymmetrical boudinage of twinned crystals (circled areas); shear is in plane of photograph.

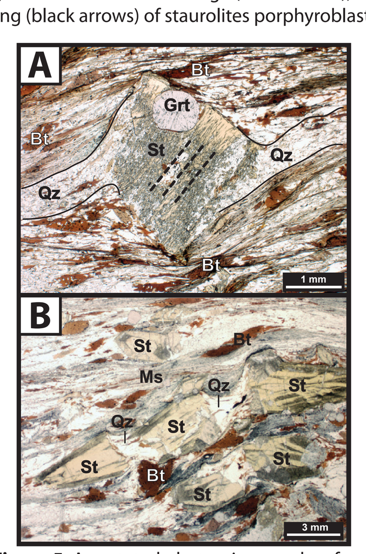

Figure 5. Annotated photomicrographs of Appleton Ridge Formation samples. A) Staurolite δ- clast displaying dextral shear sense, planar inclusion texture, and a garnet inclusion. B) Elongate staurolites displaying asymmetric boudinage. Bt=biotite, Grt=garnet, Ms=muscovite, St=staurolite, Qz=quartz.

– Matrix composed of: biotite, muscovite, quartz, and plagioclase
  • Qz: SPO with poor CPO
– Youngest fabric (S_3) wraps staurolite grains
– Staurolite displays multiple growth zones and internal inclusion fabrics
– Boudin fractures crosscut all internal textures
– Boudinage in most commonly asymmetric
  – optical estimates indicate >25° relative rotation

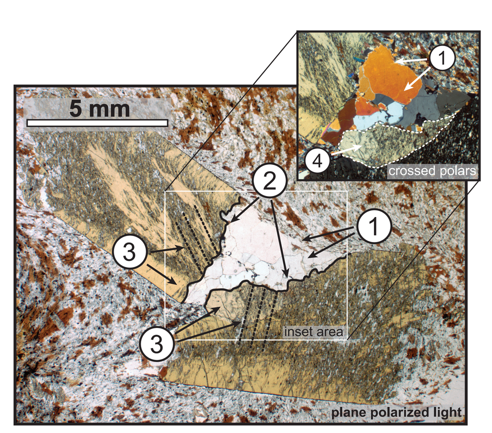

Figure 6. Criteria used for optical correlation of boudinaged staurolite fragments. (1) Chiefly monomineralic zones between staurolite fragments. Zones exhibit large grain sizes relative to and sharp boundaries with the matrix. (2) Matching fracture patterns at fragment margins. (3) Internal inclusion fabrics (black dotted lines) and/or growth zones. (4) Remnant penetrative twin intersections (outlined in white dotted line).

IV. Electron backscatter diffraction (EBSD) Results

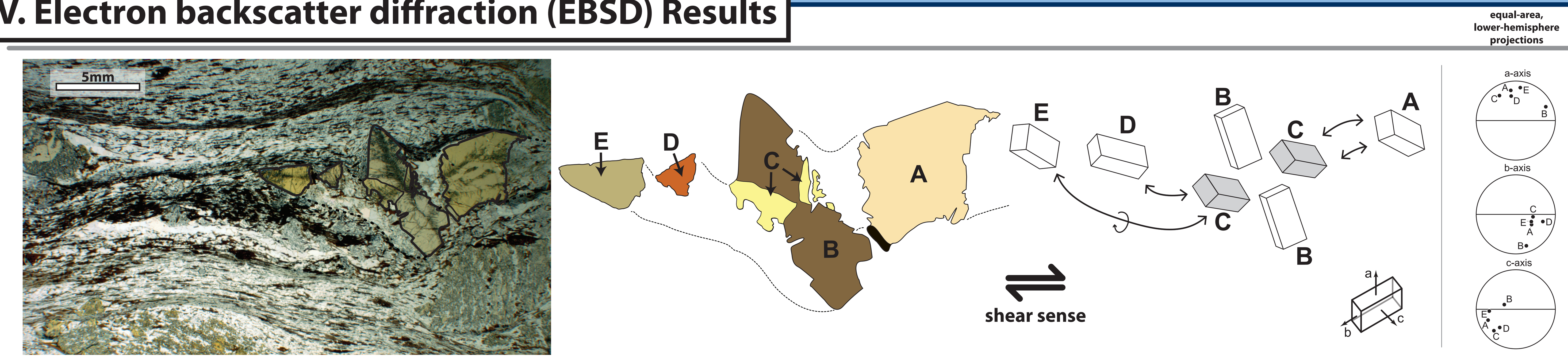

Sample # [reference Orientation]	Relative misorientation angle (degrees)			
12-b2 [C]	A-C	B-C	D-C	E-C
	23	89*	26	39

* = twin relationship

Relative Misorientation Axes [reference orientation]

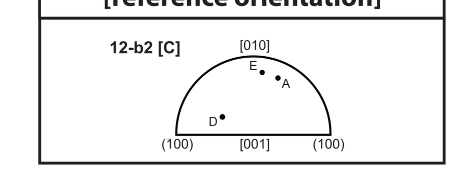

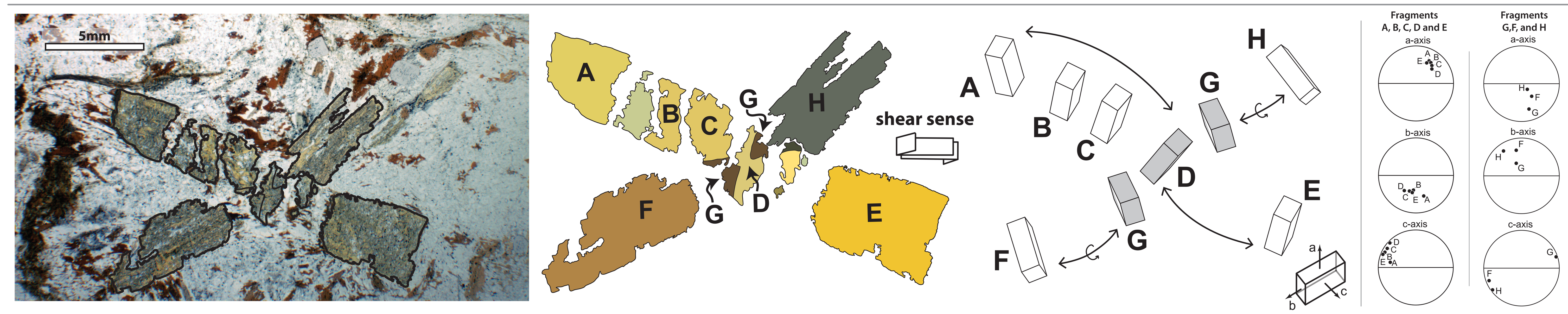

Sample # [reference orientation]	Relative misorientation angle (degrees)			
10S [D]	A-D	B-D	C-D	E-D
	39	24	15	22
10S [G]	F-G	H-G	D-G	
	31	48	119*	

* = twin relationship

Relative Misorientation Axes [reference orientation]

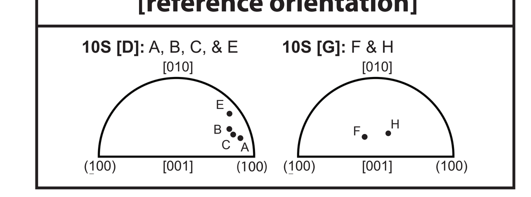

Photomicrographs w/Outlines of Boudinaged Staurolite | Enlarged Outlines w/Orientations Identified | Unit Cell Representations | Axial Orientations | Relative Misorientation Angles/Axes

V. Discussion of Microstructural Analysis

– Asymmetric boudinage and rotation *require* shear coupling
– EBSD indicates relative rotation of staurolite grain is complex in 3-D
  • Observed relative misorientations range from14 to 65° with an average of 38°
– **Large magnitudes of the observed rotation occurred out of the shear plane**
– Differential fragment rotations likely resulted from:
  (1) initial grain shape and orientation
  (2) grain shapes which developed as boudinage progressed
  (3) local grain proximity & flow perturbations

VI. Finite Element Numerical Models

– Observations above (see section IV) indicate shear, rotation, and viscous coupling
– Models used to test the influence of microstructural and rheological variation on bulk strength and inclusion-matrix shear coupling
– Calculations utilized ELLE (Bons et al., 2008), Basil (Houseman et al., 2008), and the following equation:

$$\eta_{bulk} = \frac{\tau_{xy}}{(\partial u_x/\partial y)_v} \; ; \; (\partial u_x/\partial y)_v = 1$$

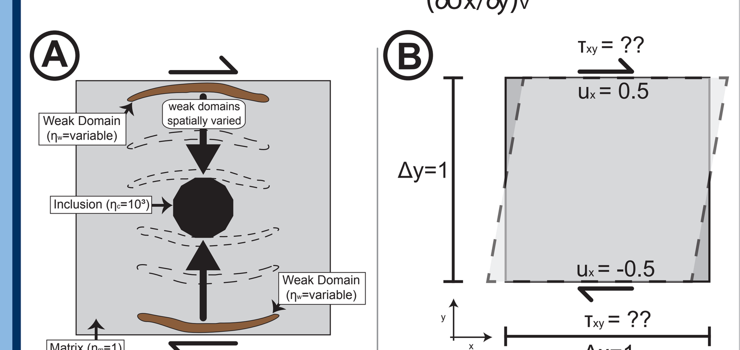

Figure 7. (A) Schematic representation of geometries and viscosity distributions used in the sensitivity analysis. (B) Geometric representation of dimensionless bulk effective viscosity calculation method. Model output includes the shear traction necessary to perform the deformation and the instantaneous distribution of kinematic parameters (after Gerbi et al., 2010).

Array 1

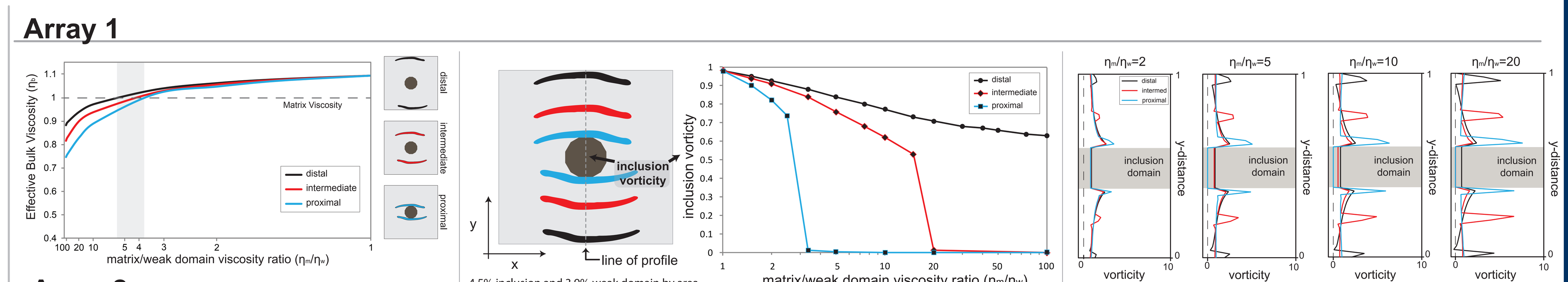

Array 2

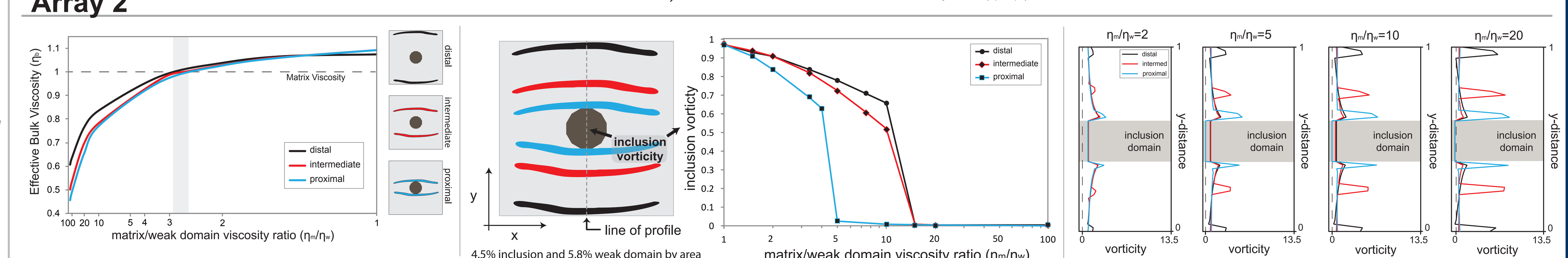

Bulk Viscous Strength Results | Inclusion Vorticity | 1-D Vorticity Profiles at x=0.5 and y=0 to 1

Dimensionless Vorticity Results

VII. Numerical Results

– Threshold for bulk weakening (i.e., $\eta_b \leq 1$) is relatively discrete (η_m/η_w=2.8-5.5) for all weak domain distributions
– Bulk strength depends on proximity of weak and strong domains, particularly with large competancy contrasts
– Inclusion vorticity depends *strongly* on the spatial proximity and relative strength of weak and strong domains
  • kinematic decoupling occurs at: $\eta_m/\eta_w \approx$ ***2.5-5*** (proximal) $\eta_m/\eta_w \approx$ ***15-20*** (int. to distal)
– The threshold for bulk weakening (i.e., $\eta_b \leq 1$) does not coincide with kinematic decoupling
  • i.e., **bulk weakening does not equate to kinematic decoupling of porphyroblasts**

VIII. Conclusions

– Microstructural analysis indicates that formerly continuous staurolites grains boudinaged and rotated relative to one another synchronous with bulk non-coaxial shear in the matrix
– Relatively minor microstructural variations of rheological heterogeneity results in heterogeneous distributions of kinematic parameters, localization, and non-ideal rotational behavior of rigid porphyroblasts
– The bulk strength of porphyroblastic rocks is dependent on the microstructural distribution and spatial proximity of rheologically distinct fabric elements
– Our analyses suggest that inherent microstructural and rheological heterogeneity can affect interpretations of the kinematic vorticity number that are derived from porphyroblast grain or internal inclusion-trail orientations (e.g., Passchier, 1987)

IX. Works Cited

Bons, P.D., Koehn, D., Jessell, M.W., 2008. Microprocess Simulations. In: Bons, P.D., Koehn, D., Jessell, M.W. (Eds.), Microdynamics Simulation. Lecture Notes in Earth Sciences. Springer, Berlin.
Gerbi, C., Culshaw, N.G., Marsh, J.H., 2010. Magnitude of weakening during crustal-scale shear zone development. Journal of Structural Geology 32, 107-117.
Gerbi, C., West Jr., D.P., 2007. Use of U-Pb geochronology to identify successive , spatially overlapping tectonic episodes during Silurian-Devonian orogenesis in south-central Maine, USA. Geological Society of America Bulletin 119, 1218-1231.
Groome, W.G., Johnson, S.E., 2006. Constraining the relative strengths of high-grade metamorphic rocks using foliation refraction angles: an example from the Northern New England Appalachians. Journal of Structural Geology 28, 1261-1276.
Hibbard, J.P., van Staal, C.R., Rankin, D.W., and Williams, H., 2006, Litho- tectonic map of the Appalachian orogen (South), Canada–United States of America: Geological Survey of Canada Map 02096A, 2 sheets, scale 1:1,500,000.
Houseman, G., Barr, T., Evans, L., 2008. Basil: computation of stress and deformation in a viscous material. In: Bons, P.D., Koehn, D., Jessell, M.W. (Eds.), Microdynamics Simulation. Lecture Notes in Earth Sciences. Springer, Berlin, 139-154.
Johnson, S.E., Lenferink, H.J., Price, N. A., Marsh, J.H., Koons, P.O., West, D.P., Beane, R., 2009. Clast-based kinematic vorticity gauges: The effects of slip at matrix/clast interfaces. Journal of Structural Geology 31, 1322-1339.
Passchier, C.W., 1987. Stable positions of rigid objects in non-coaxial flow--a study in vorticity analysis. Journal of Structural Geology 9, 679-690.